Journal of Water Process Engineering 47 (2022) 102639

Contents lists available at ScienceDirect

Journal of Water Process Engineering

journal homepage: www.elsevier.com/locate/jwpe

Co@N-C nanocatalysts anchored in confined membrane pores for instantaneous pollutants degradation and antifouling via peroxymonosulfate activation

Yuhang Han [1], Bin Jiang [1], Congcong Zhang, Longfei Zhang, Luhong Zhang, Yongli Sun, Na Yang [*]

School of Chemical Engineering and technology, Tianjin University, 300350 Tianjin, China

ARTICLE INFO

Keywords:
Catalytic membrane
Nitrogen doped carbon
Instantaneous degradation
Advanced oxidation process

ABSTRACT

Heterogeneous advanced oxidation processes (AOPs) are promising to generate reactive oxygen species (ROS) for the destruction of aqueous organic pollutants via peroxymonosulfate (PMS) activation. However, practical treatment suffers from both mass transfer limitations and the drawback of heterogeneous catalyst. Herein, we overcame the challenges by dispersing cobalt nanoparticles encapsulated nitrogen doped carbon shells (Co@N-C) within the pores of ultrafiltration membrane uniformly and tightly. The nitrogen doped carbon shells not only provided electron to active PMS, but also suppressed the aggregation of the nanoparticles. Furthermore, the Co@N-C nanocatalysts were anchored in confined membrane pores to enhance the catalytic efficiency. As expected, the membrane pores concentrated the pollutant and reactive oxygen species, leading excellent instantaneous decomposing rate. The Co@N-C doped polyvinylidene fluoride (PVDF/Co@N-C) membrane attained 99.3% tetracycline hydrochloride (TC, 20 mg·L^{-1}) degradation in 60 min. Remarkably, since the higher hydrophilicity, the permeation flux of PVDF/Co@N-C membrane was enhanced to 636.0 L·m^{-2}·h^{-1}, improving the wastewater treatment efficiency. The membrane flux recoveries rate was 85%and the degradation stability was excellent after PMS-based cleaning process. In addition, the degradation sites of TC and possible degradation pathways were explored with density functional theory (DFT) calculations and liquid chromatography-mass spectrometry (LC-MS) analysis. This work provides the potential application of the catalytic membrane in water remediation.

1. Introduction

Recently, with the dwindling of water, the presence of antibiotics in the aquatic environments has emerged as a major concern [1,2]. Tetracycline hydrochloride (TC) is widely used in veterinary medicine and is discharge to the environment from both human and agricultural sources because of the non-biodegradable characters [3,4]. The residues left in environment can develop antibiotic-resistant pathogens and cause serious problems to human health [5].

Sulfate radical-based advanced oxidation processes (SR-AOPs) are aqueous phase oxidation methods leading to partial oxidation and mineralization of pollutant [6–8]. Because of the redox cycle through the transition of electronic state, the multivalent transition metals could accelerate peroxymonosulfate (PMS) activation to generate reactive oxygen species (ROS) [9,10]. To generate the radical, transition metals (TMs) and metal oxides are considered to be an exciting alternative which is more economical compared to the energy-based methods, such as ultrasound, UV, etc. [11,12]. Carbon-based material catalysts were extensively studied because of the unique electron transfer properties [13–15]. Moreover, some studies proved that doping nitrogen could adjust the chemical property of graphitic shell and provide abundant new active sites [16,17]. TMs nanoparticles encapsulated nitrogen doped carbon shells (TMs@N-C) with elaborated structures could perform efficient catalytic performance and avoid metal ions leaching. Wang et al. designed cobalt and nitrogen co-doped porous carbon that was highly efficient than Co-C and homogeneous Co^{2+} for activating PMS to remove phenol [18]. Xue et al. probed the different physics and catalytic properties of Co@N-C nanoparticles that were produced by

* Corresponding author at: School of Chemical Engineering and Technology, Tianjin University, Tianjin 300072, China.
E-mail address: yangnayna@tju.edu.cn (N. Yang).
[1] These authors contribute equally to this work.

https://doi.org/10.1016/j.jwpe.2022.102639
Received 18 November 2021; Received in revised form 20 January 2022; Accepted 3 February 2022
Available online 19 February 2022

pyrolyzing ZIF-67 at different temperature [19]. Though the carbon shells could suppress the aggregation, the nanoparticles agglomerate inevitably, which affects catalytic activity. And the poisonous metal leaching was also the problem need to solve of the heterogeneous catalyst.

Membrane separation is widely used in wastewater treatment owing to the advantage of easy operation and high selectivity [20,21]. And due to the tortuous pathways of membrane pore size, the enhanced mass transfer which depends on mass flow offers high reaction efficiency. Now the catalytic membrane, coupling of AOPs and membrane separation processes, has become an emerging water treatment technology [3,22–25]. The catalytic membrane not only solves the shortcoming of membrane for small-molecular contamination but also overcomes the aggregation and re-utilization of nano-catalysts for practice use. Li et al. built poly-dopamine and ZIF-67 decorated polypropylene membrane with catalysis property and excellent membrane properties [26]. There are high loading cites of catalysts in the membrane pores, improving the catalytic efficiency due to the enhanced mass transfer. The mass transfer enhancement is because of the tortuous pathways of the membrane pores, which could high-efficiently concentrate and converse pollutants [27]. Constructing a membrane with suitable structure to load nano-catalysts is the key to accomplish high and constant catalytic performances [28]. Lin et al. enable in-situ growth of Prussian blue micro-crystals in the PVDF membrane micro-clusters which achieved the high degradation efficient and instantaneous decomposing of multiple pollutants [29]. However, due to its narrowed pore congested by nanoparticles, more catalyst loading would make catalytic membrane flux lower, which is an important factor in the practical operation. What's more, metal ion leaching of transitional metal catalyst significantly affects its stability and may cause secondly pollution. Embedding metal catalyst on porous carbon shell could not only optimize the stability of the catalyst, but also enhance catalytic activity due to the accelerated interaction between metal sites and carbon shell. Besides, carbon based catalytic often possesses attractive hydrophilicity, which is beneficial to improve the permeability of membranes.

In this paper, Co@N-C nanoparticles were synthesized by pyrolyzing ZIF-67 nanocrystals and then doped in PVDF membrane for wastewater treatment via synergistic effect of catalytic oxidation, separation and adsorption. PVDF/Co@N-C catalytic membrane achieved high removal efficiency of TC with negligible leaching of Co, treating simulated wastewater including TC and humid acid (HA). Simultaneously, the effect of different operation conditions to the degradation was investigated. We identified the ROS involved and proposed reaction mechanisms of Co@N-C for PMS activation. Radicals and nonradicals pathways were both verified and $^1O_2$ was major contributor. Finally, we explored the degradation sites of TC and possible degradation pathways by DFT calculation. This work is meaningful for the application of these novel catalytic membranes in practical applications.

2. Experimental section

2.1. Materials and experimental methods

We pyrolyzed ZIF-67 to prepare Co@N-C nanoparticles and doped the nanoparticles in the membrane (Scheme S1). The specific prepare processes are in the Supplementary material.

2.2. Performance of catalyst particles

The catalytic performance was evaluated by the removal ratio and removal rapid of the TC via PMS activation. 0.01 g catalyst was put into the 100 mL 20 ppm TC solution simultaneously with magnetic stirring under a 25 °C water bath. After rotated for 30 min, we could get the adsorption performance of catalyst nanoparticles. Then we added 1.0 mM PMS into the solution and withdrew quantitative solution to test at certain time intervals. The concentration of TC could be measured using the UV–vis spectroscope with the wavelength at 357 nm.

Besides, the TC degradation reaction could be approximated as first-order reaction. The kinetics equation was used to analyze the reaction rate (Eq. (1)).

$$ln\frac{C}{C_0} = -kt \tag{1}$$

where C_0 is the initial concentration of TC solution (mg·L^{-1}) and C is the tested one, k means the reaction rate constant (min^{-1}), t means the reaction time (min).

2.3. Evaluation of membrane performance

The degradation experiments of TC were used a homemade cross-flow filtration device under cyclic conditions (shown in Fig. S1). Batch experiments were carried out to get the degradation efficiency of TC solution under different conditions (PMS dosage, TC concentration, pH, temperature, etc.).

The water flux was measured to clarify the permeability of the CM using a homemade cross-flow model. After 30 min pre-compaction of the membranes at 0.12 MPa, the pressure was decreased to 0.1 MPa and pure water flux (J) of the membrane was recorded according to Eq. (2).

$$J = \frac{V}{A \times \Delta t} \tag{2}$$

where J is the water flux of membrane(L·m^{-2}·h^{-1}), V is the volume of permeate water (L), $\triangle t$ is the filtration time (h), A is the effective membrane area (4.9×10^{-4} m^2).

Membrane porosity (φ) was obtained using Eq. (3).

$$\varphi = \frac{M_w - M_d}{\rho_w A d} \tag{3}$$

where M_w and M_d (g) are the weight of wet and dry membrane, respectively, ρ_w (g·cm^{-3}) is the density of pure water, A (cm^2) is the membrane area, and d (cm) is the membrane thickness.

The HA rejection ratio of the catalytic membrane elucidated the separating performance to the wastewater treatment. The HA solution was circulated in a cross-flow model. The concentration of HA could be measured using the UV–vis spectroscope with the wavelength at 254 nm. The HA rejection ratio (R) was calculated by:

$$R = \frac{C_o - C}{C_0} \tag{4}$$

where C_0 is the initial concentration of HA solution (mg·L^{-1}) and C is the tested.

In the anti-fouling experiments, after 30 min pre-compacted at 0.12 MPa, the deionized water flux of membrane (J_{w1}) was measured at 0.1 MPa for 30 min. Then HA solution flux was measured for 30 min. Afterwards, the fouled membrane was rinsed by PMS solution. The pure water flux of the recuperated membrane (J_{w2}) was recorded for another 30 min. Flux recovery rate (FRR) was introduced to evaluate the anti-fouling property of membranes and calculated using:

$$FRR = \frac{J_{w2}}{J_{w1}} \times 100\% \tag{5}$$

3. Results and discussion

3.1. Structure and morphology of catalytic particles

The morphology of ZIF-67 and Co@N-C are shown in Fig. 1a, b. It can be seen that the ZIF-67 were regular dodecahedron morphology with a diameter about 300 nm. In addition, the FT-IR diagram further shows the Co—N bonding characteristic peak of ZIF-67 nanoparticles (shown in Fig. S2). After the pyrolyzing, it could be observed that the

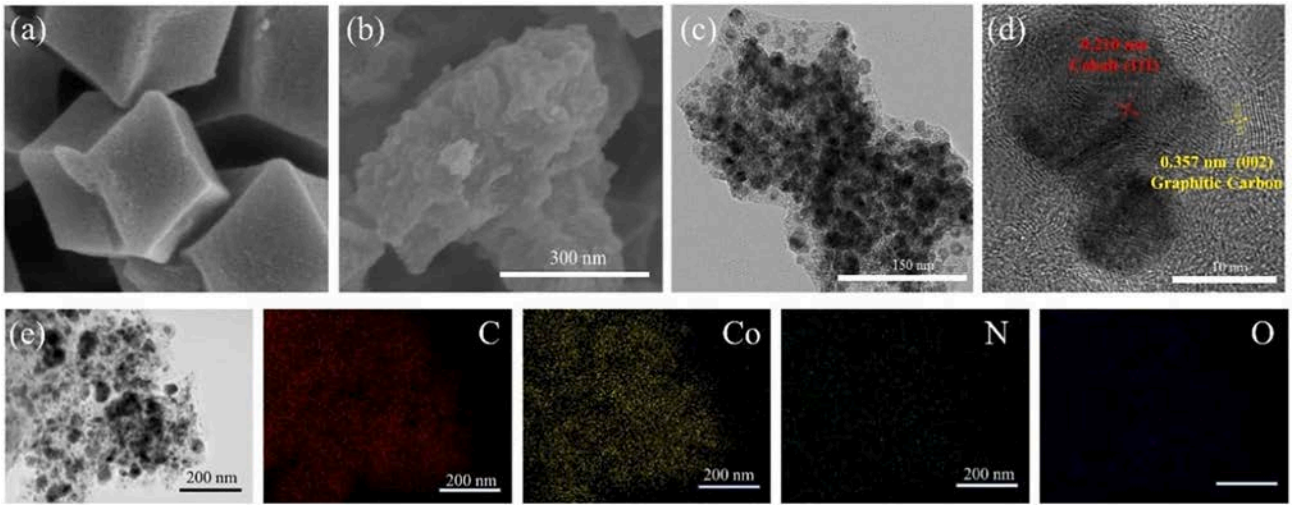

Fig. 1. SEM image of (a) ZIF-67 and (b) Co@N-C. (c) TEM image and (c) HRTEM image of Co@N-C. (e) Element mapping of C, Co, N and O for Co@N-C.

dodecahedron structure of ZIF-67 was not collapsed and the dispersed Co@N-C particles with a size around 20 nm were stacked on the surface. Compared to ZIF-67, the pyrolyzed catalyst provided higher surface area. Fig. 1c shows the TEM image of Co@N-C particles, further confirming the morphology. It was found that nanoparticles exhibited good sphericity with a particle size around 20 nm, which was consistent with the SEM result. Fig. 1d exhibits the HRTEM image of Co@N-C, manifesting that Co nanoparticle was well coated with a graphite carbon shell with a typical core/shell structure, which was beneficial for enhanced stability to suppress the leaching of metal. Moreover, the HRTEM analysis demonstrates ca. 0.21 nm and 0.35 nm of the interplanar spacing, corresponding to the (111) crystalline plane of zero valence Co and the (002) crystalline plane of graphitic carbon [30,31]. EDS mappings of Co@N-C (shown in Fig. 1e) illustrate the uniform distribution of the Co, O, N in nanocrystals.

The XRD patterns of the catalytic particles are displayed in Fig. 2a, in which the peaks at $2\theta = 44.5^{\circ}$, 51.7°, 75.4° can be corresponding to (111), (200) and (220) crystalline planes of the pure structure of $Co@C_x$ (JCPDS No. 89-4307), respectively[32]. And the existence of broad peak at $2\theta = 22^{\circ}$ was due to the influence of Si base. In addition, the peak centered at 26° can be ascribed to the typical amorphous carbon (002) plane ((JCPDS No. 75-1621)) [19]. No other crystal peaks were discovered, confirming the successful construction of Co@N-C. Fig. 2b displays the nitrogen adsorption−desorption isotherms of Co@N-C particles, with a typical type IV isotherm, demonstrating the existence of a large number of disordered mesopores [33]. The specific surface area (SSA) of the nanoparticles was given as 258.9 m^2/g. Besides, the pore size of Co@N-C exhibited a range from 2 to 80 nm (Fig. 2c). The nanoparticles with high SSA exposed more active sites, improving the catalytic efficiency.

The surface elemental composition and chemical states of Co@N-C were further researched by XPS analysis (Fig. 2d). It revealed that the prepared Co@N-C mainly consisted of C (87.1 at. %), N (5.18 at. %), O (5.75 at. %) and Co (1.98 at. %) elements. As revealed in Fig. 2e, the C 1s XPS spectrum was deconvoluted into three peaks located at 284.78, 285.3 and 287.1 eV, corresponding to graphitic C, C—N and C═O respectively [34]. As shown in Fig. 2f, the high-resolution spectrum peaks of O 1s located at 531.6 and 529.2 eV, corresponding to hydroxyl oxygen (—OH) (86.51%) and lattice oxygen (O_{latt}) (13.49%), which indicates the slight oxidation on the Co particles surface [35]. The N 1s spectrum in Fig. 2g was curve-into three peaks located at 398.1, 400.2 and 402.5 eV, associating with pyridinic-N (48.47%), pyrrolic-N (36.40%) and graphitic-N (15.13%), respectively. And of these types of N, some researchers have proved that doping graphitic N can speed up the electron transfer in carbon materials, which was beneficial to enhance the reactivity to activate PMS [16,36]. Fig. 2h provides the deconvolution of Co 2p spectra. A high-resolution peaks of Co $2p_{3/2}$ appeared at the binding energies of 777.9, 779.5 eV, corresponding to Co—O bond (8.73%) and Co^0 (91.27%), which also indicated the weak surface oxidation of Co atoms [37]. The zero-valent Co has more rapid reaction rate with PMS due to the unique electronic properties [36].

3.2. Catalytic evaluation of catalytic particles

As shown in Fig. 3a, the catalytic degradation efficiencies of Co@N-C catalysts for TC removal via activation of PMS were evaluated. And control experiments were performed to compare the eliminating efficiencies of various catalytic system for TC. The absorption of the TC on the catalyst surface was obviously neglectable. With PMS addition alone, 40% of TC was removed in 60 min, illustrating that self-decomposition of PMS also contributed a part to the TC degradation. Further, in the system containing the Co@N-C particles and PMS, a rapid degradation is observed with the activated PMS, removing 99% TC within 10 min. Pseudo-first-order kinetics equation of different system were fit to determine the kinetic constant of the TC degradation and exhibited in Fig. 3b. The k value of Co@N-C /PMS system was 0.55 min^{-1}, larger than that of PMS and only Co@N-C system, demonstrating the ultrafast catalytic efficiencies of the catalyst/PMS system.

3.3. Separation performance and permeability of CM

With regards to the membrane technology to treat wastewater, it is significant to examine the separation performance and the permeability, which determine the cleaning efficiency of the wastewater [38]. For the mixed matrix CM, we should determine the effect of the addition of the mixed Co@N-C particles. Therefore, we carried out experiments to examine the effect of different amount of Co@N-C on the CM. Fig. S3 shows the SEM images of the membranes cross-section with different Co@N-C content. It is clearly observed that there is an asymmetric structure in the cross-sectional SEM images. Between the dense top layer and the cell pores bottom support, the sublayer with finger-like pores made the membrane flux larger. The SEM images showed that PVDF membranes loaded with Co@N-C particles have longer finger-like pores, with thinner cell-like bottom support. As Co@N-C introduced, the viscosity of casting solution increased. As a result, the elongation of finger-like channels and the enlargement of visible pores on surface are obtained. And the surface pores are larger and denser than those of PVDF membrane, too (Fig. S4). The hydrophilicity effect of Co@N-C could

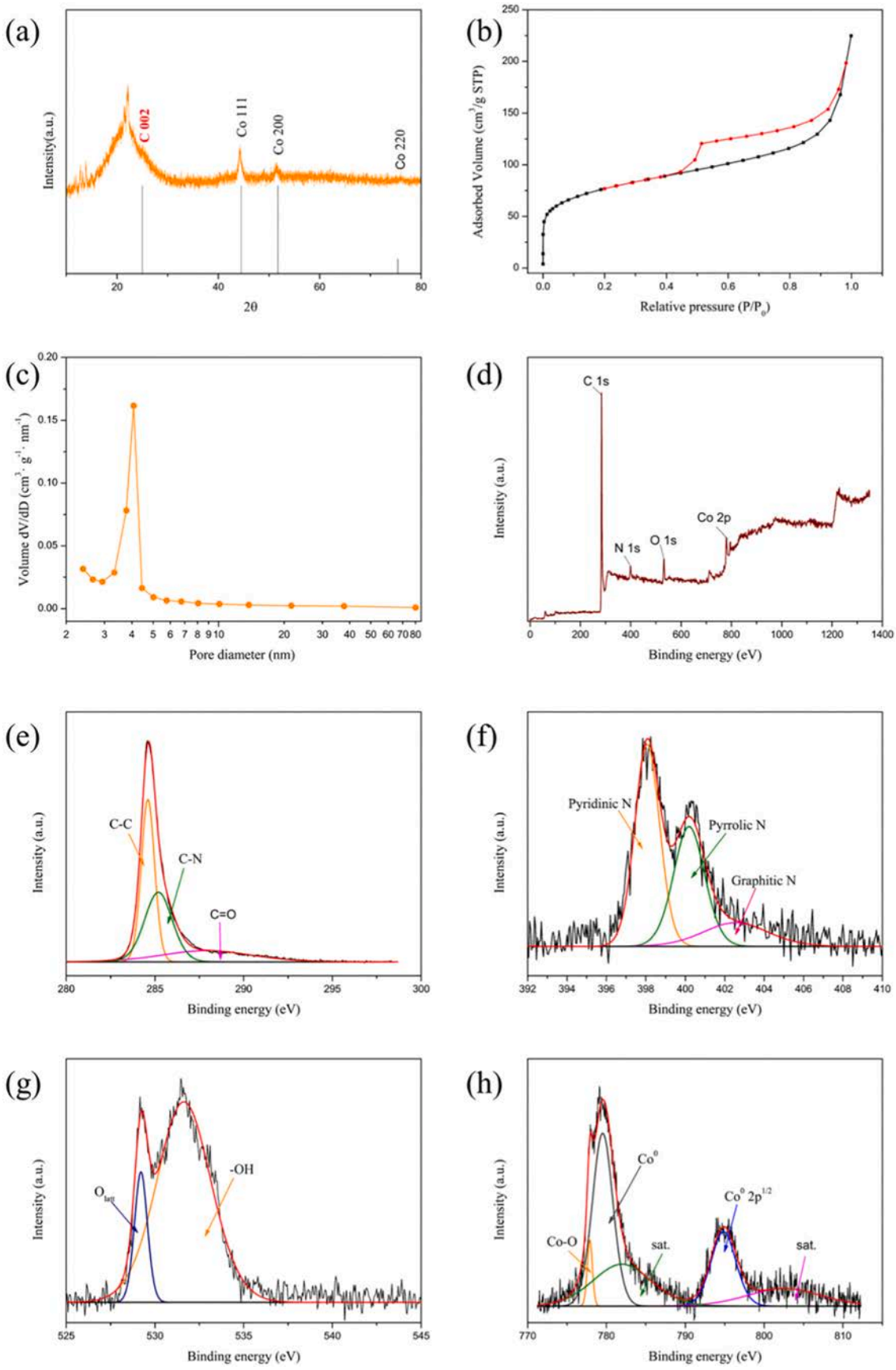

Fig. 2. (a) XRD patterns of Co@N-C. (b) N_2 adsorption-desorption isotherms and (c) homologous pore size distribution of Co@N-C. (d) XPS map and (e) the high-resolution C 1s XPS spectra, (f) N 1s XPS spectra, (g) O 1s XPS spectra and (h) Co 2p XPS spectra of Co@N-C.

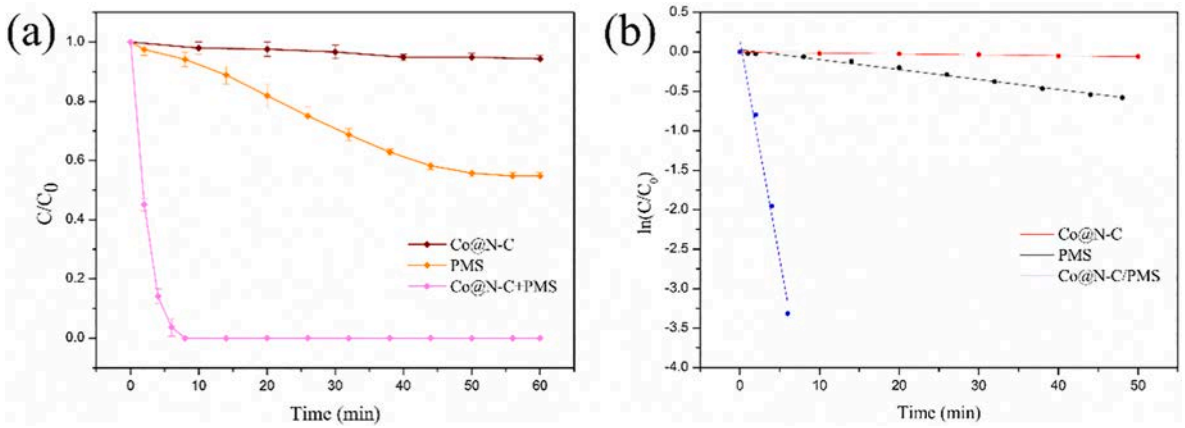

Fig. 3. (a) Degradation effect and (b) Pseudo-first order kinetic modeling of different system for TC. Reaction conditions: TC: 20 ppm, catalyst dosage: 0.02 $g{\cdot}L^{-1}$, PMS dosage: 1.0 mM, T = 25 °C and pH = 7.0.

increase the exchange phase-inversion, making the membrane have a higher porosity (Fig. 4a) [39,40]. But when the Co@N-C content is greater than 3 wt%, the viscosity of the casting solution is higher, reducing the porosity of the membrane [41]. According to pore size distribution on the surface, we could get the average pore size and size distribution (Table S2). The average surface pore size of PVDF/Co@N-C3 membrane was bigger than those of others. The water flux of PVDF/Co@N-C3 (636.0 $L{\cdot}m^{-2}{\cdot}h^{-2}$) is larger than that of PVDF/Co@N-C5 (389.5 $L{\cdot}m^{-2}{\cdot}h^{-2}$) on account of a large number of Co@N-C particles, with a little decrease of HA rejection (from 97.53% to 96.44%). In addition, the introduction of carbon materials also brings improvement in hydrophilicity, the water contact angle decreasing from 112° to 55° (Fig. S5). Furthermore, FT-IR spectra of the PVDF and PVDF/Co@N-C membrane were added (Fig. S6). It could be seen that there is no difference in the peaks between the membranes. The particles of the mixed matrix membrane are embedded in the pores of the film, and no obvious change after adding particles can be seen by the FI-IR spectra.

3.4. Catalytic performance of CM

The CM, integrating AOP and membrane process, also performs excellent catalytic activity. Fig. 5 presents the removal of TC in different systems with and without PMS addition. About 60% TC was removed in 60 min for the membrane in the absence of PMS. And the removal ratio was not much different between PVDF membrane with and without Co@N-C. We could infer that the adsorption of the membrane is the remove of TC is the main reason for the removal of TC. With the existence of PMS, there was an increase in the removal of TC for PVDF membranes, indicating that the PMS self-decomposition has a contribution to the TC degradation. The increase in catalytic performance was mainly due to the existence of a large number of finger-like pores, which could enhance mass transfer of target organic matters and reactive oxygen species. With the instantaneous degradation of organic contaminant, the TC removal efficiency of PVDF/Co@N-C catalytic membranes increased and over 90% removal of TC was achieved in 60 min. As the content of Co@N-C increases, the removal efficiency of TC for PVDF/Co@N-C membranes was enhanced. No matter the PVDF/Co@N-C3 or the PVDF/Co@N-C5 UF membranes, the removal of TC was all up to 99% within 40 min, though the initial TC removal rate of the membranes with more Co@N-C was higher, obviously. And the total organic carbon (TOC) removal of TC solution was tested to be 12.5% (shown in Fig. S7).

The optimizations of different parameters are depicted in Fig. 6. The effect of the PMS dosage on the TC degradation was presented in Fig. 6a. TC removal ratio was increased with increasing the PMS dosage. And when excessive PMS dosage was added to the reaction system, no significant improvement was observed. The possible reason is that $SO_4^{\bullet-}$ would self-quench under the excessive conditions [42], thus the final degradation efficiency was almost same when the PMS dosage is more than 1.5 mM. Hence, 1.5 mM PMS was selected to further experiment.

The effect of the TC concentration on its degradation was shown in Fig. 6b. The TC removal efficiency was reduced as the concentration of pollutants increases. When the TC concentration was 10 or 20 $mg{\cdot}L^{-1}$, almost 99% of the TC could be degraded eventually. However, when the pollution concentration reached 30 $mg{\cdot}L^{-1}$, the final removal rate decreased to 90%. These results demonstrated that the CM still presented excellent degradation efficiency at a higher TC concentration of

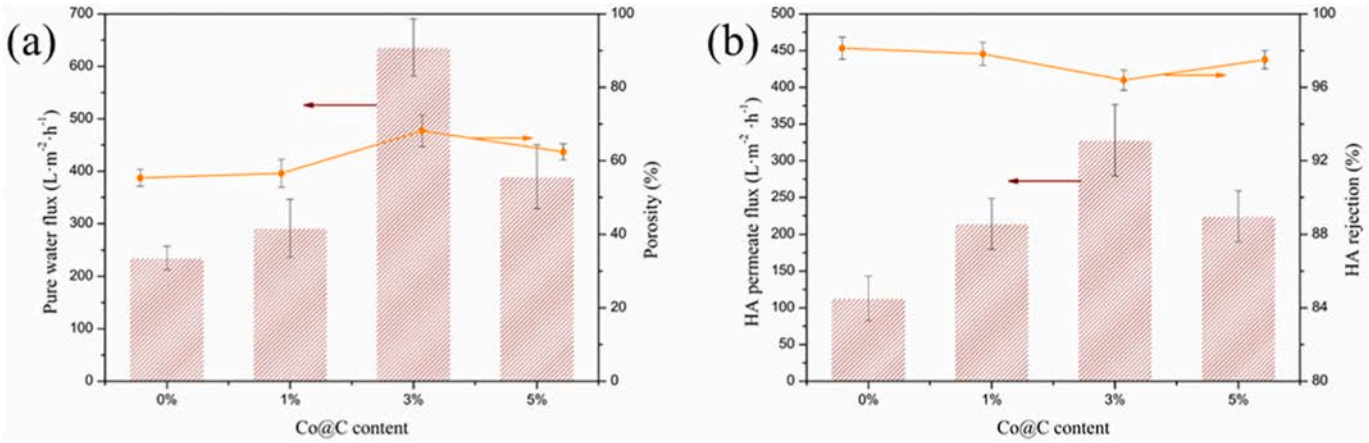

Fig. 4. Permeability of CM under various amount of mixed Co@N-C. (a) Pure water flux and porosity and (b) HA permeate flux and HA rejection.

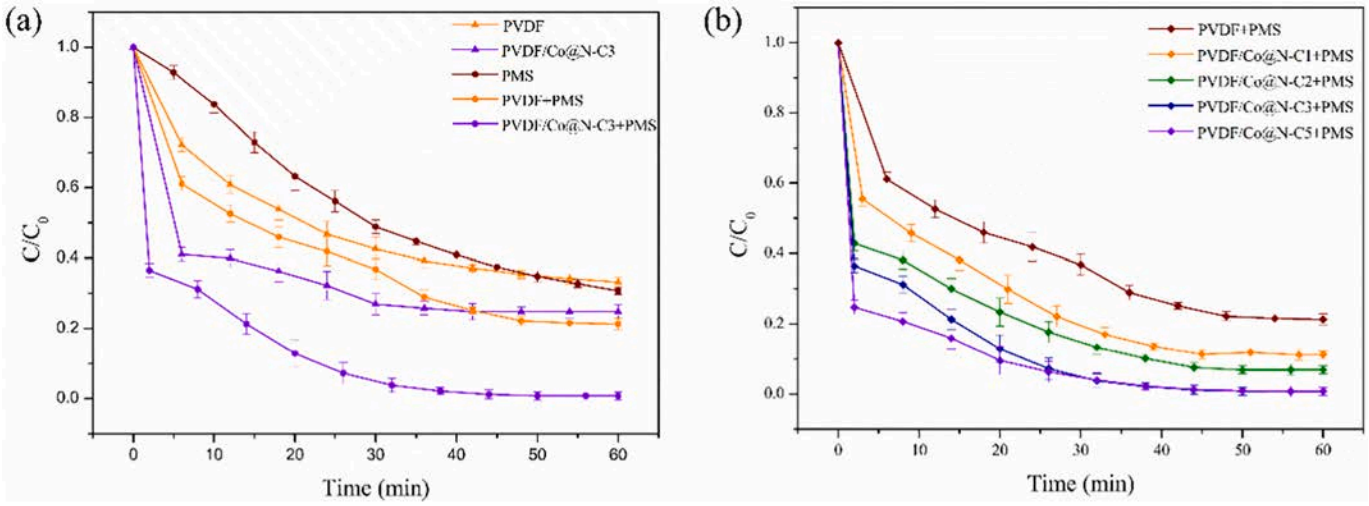

Fig. 5. (a) Effects of different system on TC removal. (b) Effects of different PVDF/Co@N-C membrane on TC removal with PMS. Reaction conditions: TC: 20 ppm, PMS dosage: 1.5 mM, T = 25 °C and initial pH = 7.0.

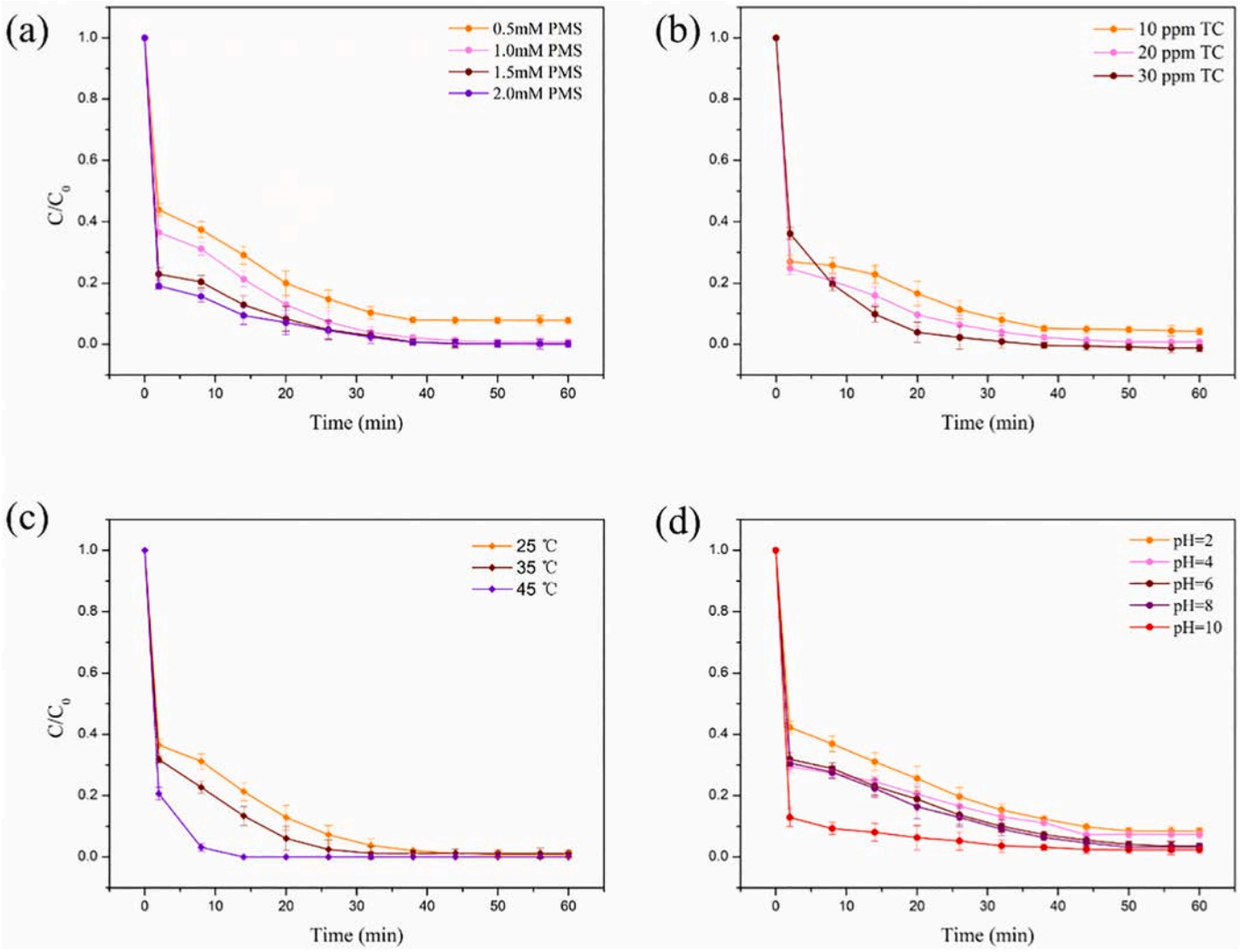

Fig. 6. Effect of different CM operation conditions. (a) PMS dosage; (b)TC concentration; (c) temperature; (d) pH value. PMS dosage: 1.5 mM, Co@N-C content: 3%, TC: 20 ppm.

20 mg·L^{-1}. The effect of the temperature on the degradation was presented in Fig. 6c. Several researchers have found that higher temperature significantly accelerated the breaking of the -O-O- bond in PMS, accelerating the generation of the active free radicals [6]. As a result, the TC degradation rate was greatly increased under high temperature. The removal efficiency of TC was up to 99% in 15 min under 45 °C. Fig. 6d displays the effect of initial pH on TC removal in the PVDF/Co@N-C3/PMS system. Before degradation reaction, the TC solution was stirred for 30 min to investigate the hydrolysis of TC. The result (Fig. S8) showed that TC would remain stable under acidic conditions, while TC would be hydrolyzed under alkaline conditions. The hydrolysis rate at pH = 11, 76% TC rapidly hydrolyzed in 5 min, is about the same as that at pH = 9. The removal efficiency of TC was obviously constrained under acidic conditions. The formation of $CoOH^+$, the key intermediate for PMS activation to product reactive radicals, was inhibited under acidic conditions, resulting in a decreased of the degradation efficiency [43]. There is little difference in the catalytic degradation rate under neutral and weakly alkaline conditions, so the catalytic oxidation efficiency of the membrane for TC at pH = 7 is better than that at weakly alkaline conditions. As for the strong alkaline conditions, because excessive OH^- in solution was beneficial to donate electrons compared with H_2O, PMS activation could be facilitated [44,45]. Although the hydrolysis degree of TC under alkaline conditions is about the same, an enhanced degradation performance also occurred at pH = 11.

3.5. Stability, recyclability and antifouling performance of CM

To better demonstrate the superiorities of the CM in practical operation, experiments were carried out to test the performance of CM. Fig. 7a showed the excellent stability of the CM, removing above 99% of the TC in the first cycle. In the subsequent experiments, the degradation efficiency of TC decreased slightly, above 90% of TC still could be removed within 60 min in 5th cycle, which reveals the good stability of the CM. The decent stability of the CM not only comes from the stability of the Co@N-C catalyst, but because the catalysts can be adhered to the membrane channels, making the catalysts difficult to lose.

As Fig. 7b shown, the antifouling performance of the PVDF membrane and PVDF/Co@N-C3 catalytic membrane was studied by comparing the membrane flux recoveries after PMS cleaning. Compared with that of pure water, the normalized HA solution flux of PVDF membrane and CM decline significantly, indicating that serious membrane fouling was caused by the blockage of pores deposited by pollutants. In the membrane operation, the reversible fouling can be easily removed and the irreversible fouling is tightly attached to the membrane surface and channels, which is robust to remove [46]. Obviously, after the intermittent cleaning process with PMS, the CM had a higher value of FRR (85.3%) in the first cycle than that of PVDF membrane (43.1%). After 3 consecutive cycles, the FRR of CM is still larger than 70%, proving that CM has good long-term antifouling performance. Based on the antifouling experimental, we could surmise that the strongly bound foulant were effectively degraded by the free radical that generated by the PMS activation.

3.6. Evaluation of metal leaching property

For cobalt-based catalysts, the leaching of cobalt ions would cause the secondary pollution issue, toxic and carcinogenic. The degradation performance of CM via PMS activation and the leaching of ions were compared with other Co-based catalyst (shown in Table S3). As seen, PVDF/Co@N-C membrane showed better catalytic performance than most of reported cobalt-based catalysts. And the Co leaching of the CM is 0.07 mg·L^{-1}, better than most of supported Co-based catalysts. We could prove that the composite membrane and the carbon shell were favorable for the declining of metal ions leaching.

3.7. Quenching experiments

Since PMS activation can generate the radical and nonradical, the useful pathways in the degradation processes should be identified. We could use several scavengers to get the dominant ROS in the further quenching experiments. Methanol (MeOH) could be employed to scavenge $SO_4^{\bullet-}$ and •OH, because it could react to the radicals with high rate ($k_{SO4^{\bullet-}} = 1 \times 10^7$ M^{-1} s^{-1}, $k_{\bullet OH} = 9.7 \times 10^9$ M^{-1} s^{-1}) [17]. While *tert*-butyl alcohol (TBA) only could be used to quench •OH, because it has a good reactivity with •OH ($k_{\bullet OH} = 6 \times 10^8$ M^{-1} s^{-1}) [47]. Furthermore, p-benzoquinone (p-BQ) was employed to scavenge $O_2^{\bullet-}$ with the reaction rate constant of $k = 1.0 \times 10^9$ M^{-1} s^{-1} [48]. The quenching experiments adding different concentrate gradient scavenger was to get the main ROS. When amount of MeOH and TBA increased from 500 mM to 2000 mM, 65%, 85% removed TC were reduced to 55% and 80% within 60 min, respectively. About 75% of removal efficiency was retained with 2 mM *p*-BQ, and 70% TC was removed with 10 mM *p*-BQ added. It was demonstrated that $SO_4^{\bullet-}$ was the dominant free radical. For the nonradical species, $^1O_2$ was generally considered to be scavenged by FFA ($k = 3.2 \times 10^7$ M^{-1} s^{-1}) [49]. Approximately 70% of TC was removed within 60 min with the addition of 2 mM FFA. When the FFA was increased to 10 mM, only 33% TC was removed. The electron-transfer between PMS and carbon materials has been also regarded as an alternative pathway to active PMS without radicals [46,50]. Yun. et al. demonstrated that the carbon nanotube (CNT)-mediated electron transfer from contaminants to PMS played major role for the degradation of contaminants [51]. In order to examine the electron transfer

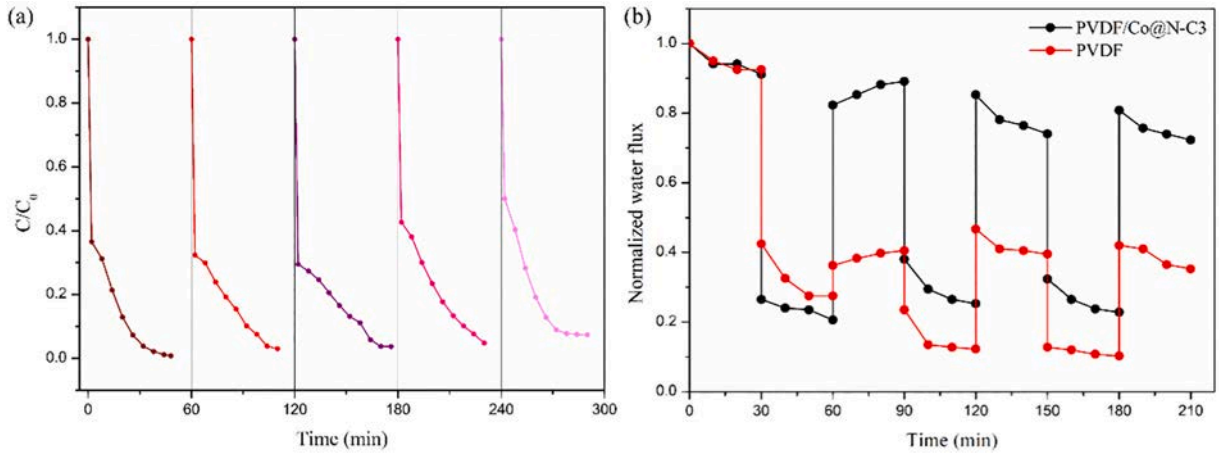

Fig. 7. (a) Stability of CM for TC removal efficiency after five cycles. (b) Anti-fouling performance of the different membranes after backwash process.

pathway of PVDF/Co@N-C/PMS system, we investigated the reaction between membrane and PMS. PMS was added to the membrane system, and TC was added after some minutes. As shown in Fig. 8h, the removal efficiency of TC was reduced after membrane operation only with PMS. If the electron transfer between TC and PMS was the main pathway, the pre-reaction would not have a signification impact on the removal efficiency [47]. the decreasing efficiency shown that Co@N-C would activate PMS to generate $^1O_2$, which could be continuously consumed. The results further confirmed that $^1O_2$ dominated the non-radical pathway. Besides, it's confirmed that the doping nitrogen in carbon, improving the conductivity, is beneficial to generate $^1O_2$, compared with the CNT/PMS system [36]. EPR spectra in Co@N-C/PMS system using DMPO for $SO_4^{\bullet-}$, •OH and $O_2^{\bullet-}$ and TEMP for $^1O_2$ were shown in Fig. 8d–f. we could propose that $SO_4^{\bullet-}$, •OH, $O_2^{\bullet-}$and $^1O_2$ were all produced in the CM/PMS system.

In general, the quenching experiments and EPR spectra suggested that the PVDF/Co@N-C/PMS activates PMS through two paths. The PMS accept an electron from catalyst to generate sulfate radicals ($SO_4^{\bullet-}$) or hydroxyl radicals (•OH) in the free radical pathway. In the nonradical pathway, the electron-transfer process happens on carbon shell surface, and singlet oxygen ($^1O_2$) is the dominant one. What's more, it could be detected that the nonradical degradation was the main pathway to degrade TC in the CM/PMS system.

3.8. Catalytic reaction mechanism and pathway

Based on the previous discussion, WE could get the contribution of free radicals and non-radicals to the process of Co@N-C activation of PMS. Some previous studies have proved that the different nitrogen doped in carbon are favorable for the absorption of different substance. Graphitic N with high electronegativity could facilitate the adsorption of negatively charged HSO_5^- [52]. And pyrrolic N could capture organic pollutants to react with radicals rapidly [36]. Besides, the membrane pore could further concentrate the pollutants and oxidative radicals to enhance the catalytic efficiency.

The possible catalytic mechanisms of Co@N-C were investigate through XPS spectra of Co@N-C before and after reaction. For Co 2p XPS spectrum, the proportion of zero-valent cobalt decreased from 91.27% to 5.66%, implying Co^0 was almost completely transformed into Co^{2+} (Fig. 9a). Meanwhile the peak of Co^{3+} appeared, and the relative content of Co^{2+}/Co^{3+} after reaction was 57.62%:36.71%, indicating the existence of the redox cycle. For N 1s, the peak of graphitic N disappeared, and the peak of oxidized N appeared after the reaction (Fig. 9b). The content of pyrrolic N increased from 36.40% to 59.43%, while that of pyridinic N decreased from 48.47% to 21.95%, relatively. The change of relative content of different N states indicated that N species played an important role during the PMS activation.

The zero-valent cobalt could directly active PMS to accelerate the generation of radicals, releasing Co^{2+} (Eq. (6)). Co^{2+} reacted with PMS and $SO_4^{\cdot-}$ was generated (Eq. (7)). And Co^{3+} could react with PMS to generate Co^{2+} to accomplish the periodic cycle of Co^{2+}/Co^{3+}. What's more, the core–shell structure and membrane pores made that Co^{3+} was deposited with Co^0 to further obtain sufficient Co^{2+} (Eqs. (8) and (9)). $SO_4^{\bullet-}$ in aqueous solution would react with H_2O/OH^- to generate amount of •OH (Eq. (10)). In addition, the π-electrons from the sp^2 C could be activated by the lone-pair electrons of the doping N [36]. The N doped carbon shell was favor to enhance the catalytic activity to stimulate PMS (Eq. (11)). Electron transfer is an important reason for the formation process of $O_2^{\bullet-}$. The reaction happened between •OH and H_2O_2 which were intermediates in the PMS activation process to generate perhydroxyl radicals ($HO_2^{\bullet}$) (Eqs. (12) and (13)). Then $HO_2^{\bullet}$ decomposed to generate radical $O_2^{\bullet-}$ (Eq. (14)). PMS anion radicals ($SO_5^{\bullet-}$) were produced by the reduction of Co^{3+} (Eq. (8)). And then $SO_5^{\bullet-}$ could be further combined to form SO_4^{2-} ions, and meanwhile produce $^1O_2$ (Eq. (15)). Moreover, $O_2^{\bullet-}$ could also interact with •OH to generate $^1O_2$ (Eqs. (16) and (17)) [17].

$$Co^0 + 2HSO_5^- \rightarrow Co^{2+} + 2SO_4^{\bullet-} + 2\bullet OH \quad (6)$$

$$Co^{2+} + HSO_5^- \rightarrow Co^{3+} + SO_4^{\bullet-} + OH^- \quad (7)$$

$$Co^{3+} + HSO_5^- \rightarrow Co^{2+} + SO_5^{\bullet-} + H^+ \quad (8)$$

$$Co^0 + 2Co^{3+} \rightarrow 3Co^{2+} \quad (9)$$

$$SO_4^{\cdot-} + H_2O/OH^- \rightarrow SO_4^{2-} + \cdot OH \quad (10)$$

$$HSO_5^- + e^- \rightarrow SO_4^{\bullet-} + \bullet OH \quad (11)$$

$$HSO_5^- + H_2O \rightarrow H_2O_2 + HSO_4^- \quad (12)$$

$$H_2O_2 + \bullet OH \rightarrow H_2O + HO_2^{\bullet} \quad (13)$$

$$HO_2^{\bullet} \rightarrow H^+ + O_2^{\bullet-} \quad (14)$$

$$2SO_5^{\bullet-} \rightarrow 2SO_4^{2-} + {}^1O_2 \quad (15)$$

$$O_2^{\bullet-} + \bullet OH \rightarrow OH^- + {}^1O_2 \quad (16)$$

$$2O_2^{\bullet-} + 2H_2O \rightarrow H_2O_2 + 2OH^- + {}^1O_2 \quad (17)$$

$$ROS + TC \rightarrow intermediates + CO_2 + H_2O \quad (18)$$

Previous studies proved that the anions in the actual wastewater could react with the generated ROS, thereby affecting the catalytic activity of TC [53]. The inhibitory effect of anions is due to not only the complex reaction with metal ions, reducing the formation and substitution of intermediate products, but also the reaction with free radicals to generate new free radicals with lower activity. Fig. 10 shows that the effect of anions on the TC degradation. The degradation efficiency of TC displayed the order of inhibitory effect on free radicals: $H_2PO_4^- > Cl^- > HCO_3^-$. The anions would quench the hydroxyl radicals and sulfate radicals and to produce weaker radicals, while $H_2PO_4^-$ could produce PO_4^{2-} in AOPs (Eqs. (19)–(23)) [54–56]. However, the initial high degradation rate in the initial reaction may be due to the alkalinity of the solution with bicarbonate anion.

$$Cl^- + \bullet OH/SO_4^{\cdot-} \rightarrow SO_4^{2-}/Cl\bullet/HClO \quad (19)$$

$$Cl^- + Cl\bullet \rightarrow Cl_2^{\bullet-} \quad (20)$$

$$HCO_3^- + \bullet OH \rightarrow SO_4^{2-} + CO_3^{\bullet-} \quad (21)$$

$$HCO_3^- + SO_4^{\cdot-} \rightarrow SO_4^{2-} + CO_3^{\bullet-} \quad (22)$$

$$H_2PO_4^- + \bullet OH/SO_4^{\cdot-} \rightarrow OH^-/SO_4^{2-} + PO_4^{2-} \quad (23)$$

To better find out the possible degradation pathway of TC, LC-MS was carried out to analyze the intermediates of TC, integrated with the favorable primary degradation sites from DFT calculations. We used B3LYP/6-3UG (d, p) method by Gaussian to conduct geometry optimization of TC, and the three-dimensional model of HOMO and LUMO frontier orbits could indicate the orbital ESP distribution (Fig. S9). Meanwhile, theoretical calculation results reveal that C—O, C═O and C—N of TC have higher FuKui Function and lower ESP value, which were preferential attacked by ROS (Table S4). Integrated with the intermediates conducted by LC-MS analysis, the possible degradation pathways of TC were deduced as shown in Fig. S10. Firstly, TC is attacked by $^1O_2$ and is converted into compound P1 (m/z = 453) through demethylation. P4 (m/z = 436), P7 (m/z = 340), P10 (m/z = 274) and P13 (m/z = 222) are generated through demethylation, deamidation and ring-opening reactions. For second pathway, P2 (m/z = 430) and P5 (m/z = 417) are produced by *N*-demethylation of TC. And through further ring opening, P8 (m/z = 362), P11 (m/z = 318), P14 ($m/$

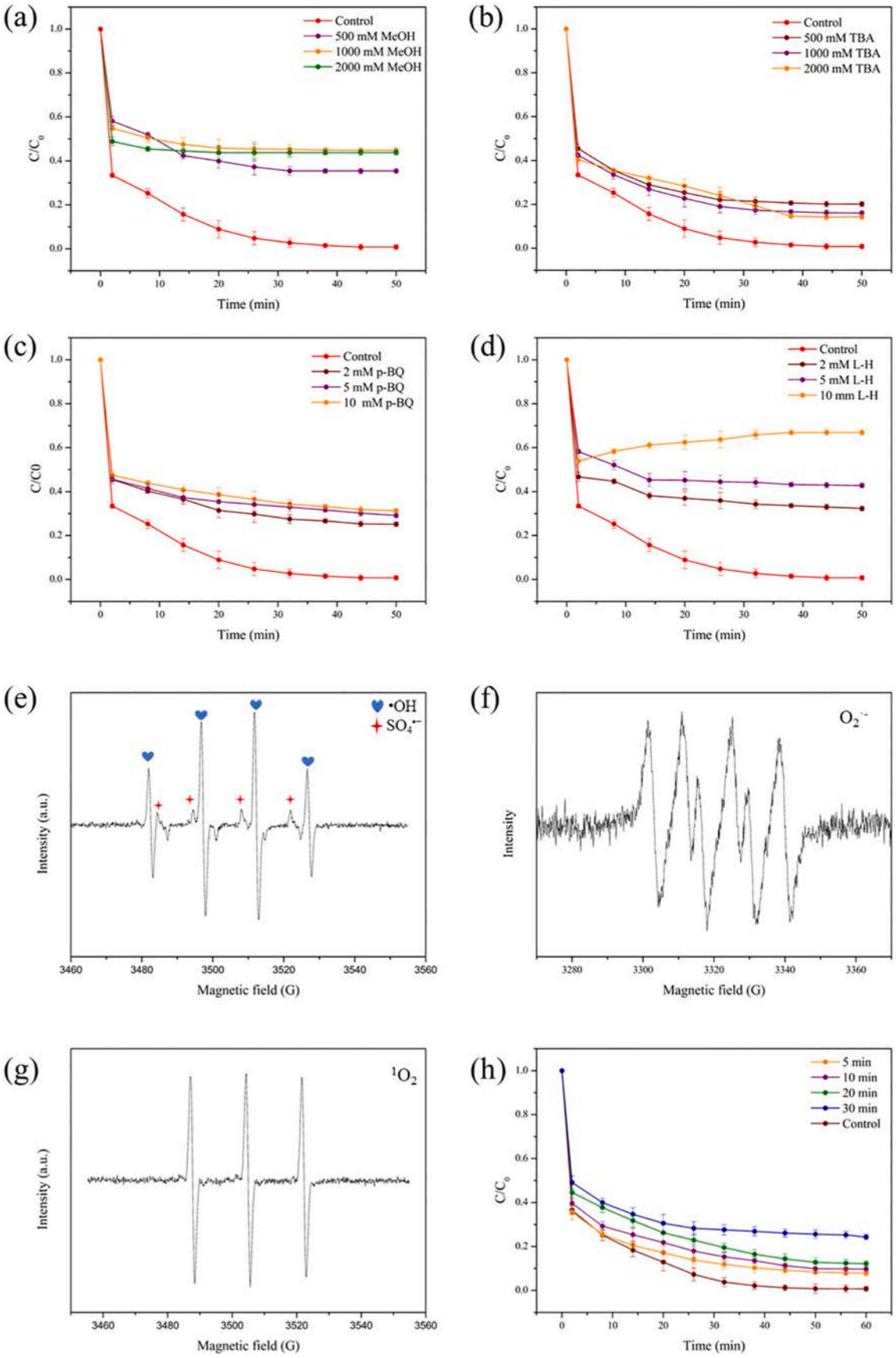

Fig. 8. (a) TC removal efficiencies with MeOH, (b) TBA, (c) p-BQ, (d) FFA. (e) EPR spectra in Co@N-C/PMS system using DMPO for $SO_4^{\bullet-}$, $^{\bullet}OH$, (f) $O_2^{\bullet-}$ and (g) TEMP for $^1O_2$. (h) The removal efficiency of TC after reaction between PMS with PVDF/Co@N-C.

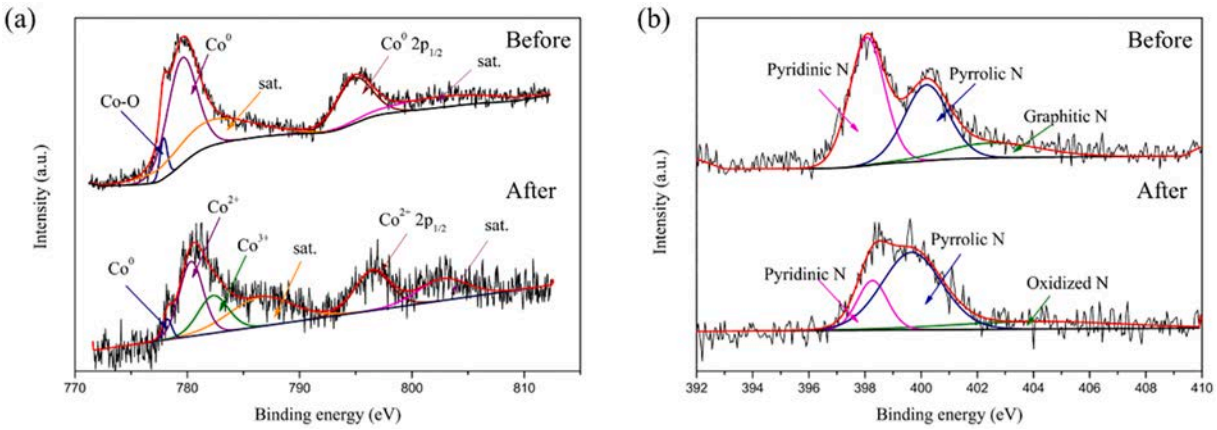

Fig. 9. (a) Co 2p, (b) N 1s XPS spectra of Co@N-C before and after reaction.

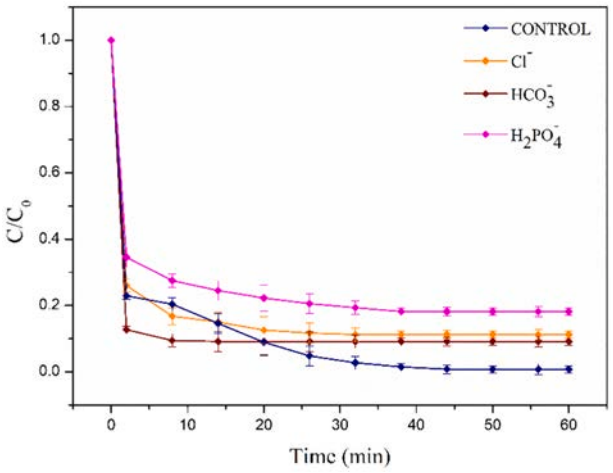

Fig. 10. The effect of anion on TC degradation.

$z = 222$) are generated. In third pathway, P3 ($m/z = 432$) is generated through dehydration process. And P9 ($m/z = 316$), P12 ($m/z = 274$), P15 ($m/z = 206$) are generated through the further *N*-demethylation reaction and ring opening. Finally, the intermediates would be further oxidized to generate small molecular organics even mineralized CO_2 and H_2O.

4. Conclusion

In this paper, Co@N-C nanocatalyst was synthesized via pyrolyzing ZIF-67 nano-particles. Then, Co@N-C nanocatalyst was anchored in confined membrane pores for water instantaneous flowing decontamination. The PVDF/Co@C3 membrane was used to remediate wastewater by the combination of cross-flow filtration and catalytic oxidation. Contaminant and ROS were confined in the membrane pore to enhance mass transfer, realizing the excellent instant degradation rate. Correspondingly, the PVDF/Co@C3 membrane was proved to possess excellent catalytic oxidation ability and separation performance with water flux 636.0 L m^{-2} h^{-1}. The active species of $SO_4^{\bullet -}$ and $^1O_2$ played dominate roles in catalytic oxidation. The degradation sites were explored with density functional theory. Meanwhile, the PVDF/Co@C3 membrane also possessed good cycle stability and antifouling performance. The PVDF/Co@C3/PMS system with catalyst constructed on pore has showed a prospective foreground for efficient wastewater treatment.

Declaration of competing interest

The authors declare that they have no known competing financial interests or personal relationships that could have appeared to influence the work reported in this paper.

Acknowledgments

The authors greatly acknowledge the financial support of National Natural Science Foundation of China (22078233).

Appendix A. Supplementary data

Supplementary data to this article can be found online at https://doi.org/10.1016/j.jwpe.2022.102639.

References

[1] J. Cao, Z.-H. Yang, W.-P. Xiong, Y.-Y. Zhou, Y.-R. Peng, X. Li, C.-Y. Zhou, R. Xu, Y.-R. Zhang, One-step synthesis of co-doped UiO-66 nanoparticle with enhanced removal efficiency of tetracycline: simultaneous adsorption and photocatalysis, Chem. Eng. J. 353 (2018) 126–137, https://doi.org/10.1016/j.cej.2018.07.060.
[2] W. Wang, Z. Zeng, G. Zeng, C. Zhang, R. Xiao, C. Zhou, W. Xiong, Y. Yang, L. Lei, Y. Liu, D. Huang, M. Cheng, Y. Yang, Y. Fu, H. Luo, Y. Zhou, Sulfur doped carbon quantum dots loaded hollow tubular g-C3N4 as novel photocatalyst for destruction of Escherichia coli and tetracycline degradation under visible light, Chem. Eng. J. 378 (2019), https://doi.org/10.1016/j.cej.2019.122132.
[3] C. Feng, L. Tang, Y. Deng, G. Zeng, J. Wang, Y. Liu, Z. Chen, J. Yu, J. Wang, Enhancing optical absorption and charge transfer: synthesis of S-doped h-BN with tunable band structures for metal-free visible-light-driven photocatalysis, Appl. Catal. B 256 (2019), https://doi.org/10.1016/j.apcatb.2019.117827.
[4] R. Daghrir, P. Drogui, Tetracycline antibiotics in the environment: a review, Environ. Chem. Lett. 11 (3) (2013) 209–227, https://doi.org/10.1007/s10311-013-0404-8.
[5] Z. Wang, H. Tang, W. Li, J. Li, R. Xu, K. Zhang, G. He, P.R. Shearing, D.J.L. Brett, Core–shell TiO2@C ultralong nanotubes with enhanced adsorption of antibiotics, J. Mater. Chem. A 7 (32) (2019) 19081–19086, https://doi.org/10.1039/c9ta06735c.
[6] W.-D. Oh, Z. Dong, T.-T. Lim, Generation of sulfate radical through heterogeneous catalysis for organic contaminants removal: current development, challenges and prospects, Appl. Catal. B 194 (2016) 169–201, https://doi.org/10.1016/j.apcatb.2016.04.003.
[7] J. Yu, L. Tang, Y. Pang, G. Zeng, H. Feng, J. Zou, J. Wang, C. Feng, X. Zhu, X. Ouyang, J. Tan, Hierarchical porous biochar from shrimp shell for persulfate activation: a two-electron transfer path and key impact factors, Appl. Catal. B 260 (2020), https://doi.org/10.1016/j.apcatb.2019.118160.
[8] G. Liao, Y. Gong, L. Zhang, H. Gao, G.-J. Yang, B. Fang, Semiconductor polymeric graphitic carbon nitride photocatalysts: the "holy grail" for the photocatalytic hydrogen evolution reaction under visible light, Energy Environ. Sci. 12 (7) (2019) 2080–2147, https://doi.org/10.1039/c9ee00717b.
[9] C. Zhang, X. Guo, Q. Yuan, R. Zhang, Q. Chang, K. Li, B. Xiao, S. Liu, C. Ma, X. Liu, Y. Xu, X. Wen, Y. Yang, Y. Li, Ethyne-reducing metal-organic frameworks to control fabrications of core/shell nanoparticles as catalysts, ACS Catal. 8 (8) (2018) 7120–7130, https://doi.org/10.1021/acscatal.8b01691.
[10] C. Xing, G. Yang, D. Wang, C. Zeng, Y. Jin, R. Yang, Y. Suehiro, N. Tsubaki, Controllable encapsulation of cobalt clusters inside carbon nanotubes as effective

catalysts for fischer-tropsch synthesis, Catal. Today 215 (2013) 24–28, https://doi.org/10.1016/j.cattod.2013.02.018.
[11] R. Yin, W. Guo, H. Wang, J. Du, X. Zhou, Q. Wu, H. Zheng, J. Chang, N. Ren, Enhanced peroxymonosulfate activation for sulfamethazine degradation by ultrasound irradiation: performances and mechanisms, Chem. Eng. J. 335 (2018) 145–153, https://doi.org/10.1016/j.cej.2017.10.063.
[12] D.B. Miklos, C. Remy, M. Jekel, K.G. Linden, J.E. Drewes, U. Hubner, Evaluation of advanced oxidation processes for water and wastewater treatment - a critical review, Water Res. 139 (2018) 118–131, https://doi.org/10.1016/j.watres.2018.03.042.
[13] X. Cheng, H. Guo, Y. Zhang, X. Wu, Y. Liu, Non-photochemical production of singlet oxygen via activation of persulfate by carbon nanotubes, Water Res. 113 (2017) 80–88, https://doi.org/10.1016/j.watres.2017.02.016.
[14] X. Duan, Z. Ao, L. Zhou, H. Sun, G. Wang, S. Wang, Occurrence of radical and nonradical pathways from carbocatalysts for aqueous and nonaqueous catalytic oxidation, Appl. Catal. B 188 (2016) 98–105, https://doi.org/10.1016/j.apcatb.2016.01.059.
[15] G. Wang, Y. Zhao, H. Ma, C. Zhang, X. Dong, X. Zhang, Enhanced peroxymonosulfate activation on dual active sites of N vacancy modified g-C3N4 under visible-light assistance and its selective removal of organic pollutants, Sci. Total Environ. 756 (2021), 144139, https://doi.org/10.1016/j.scitotenv.2020.144139.
[16] W. Ren, G. Nie, P. Zhou, H. Zhang, X. Duan, S. Wang, The intrinsic nature of persulfate activation and N-doping in carbocatalysis, Environ. Sci. Technol. 54 (10) (2020) 6438–6447, https://doi.org/10.1021/acs.est.0c01161.
[17] W. Ren, L. Xiong, X. Yuan, Z. Yu, H. Zhang, X. Duan, S. Wang, Activation of peroxydisulfate on carbon nanotubes: electron-transfer mechanism, Environ. Sci. Technol. 53 (24) (2019) 14595–14603, https://doi.org/10.1021/acs.est.9b05475.
[18] G. Wang, X. Nie, X. Ji, X. Quan, S. Chen, H. Wang, H. Yu, X. Guo, Enhanced heterogeneous activation of peroxymonosulfate by co and N codoped porous carbon for degradation of organic pollutants: the synergism between co and N, Environ. Sci. Nano 6 (2) (2019) 399–410, https://doi.org/10.1039/c8en01231h.
[19] Y. Xue, N.N.T. Pham, G. Nam, J. Choi, Y.-Y. Ahn, H. Lee, J. Jung, S.-G. Lee, J. Lee, Persulfate activation by ZIF-67-derived cobalt/nitrogen-doped carbon composites: kinetics and mechanisms dependent on persulfate precursor, Chem. Eng. J. 408 (2021), https://doi.org/10.1016/j.cej.2020.127305.
[20] E. Elele, Y. Shen, J. Tang, Q. Lei, B. Khusid, G. Tkacik, C. Carbrello, Mechanical properties of polymeric microfiltration membranes, J. Membr. Sci. 591 (2019), https://doi.org/10.1016/j.memsci.2019.117351.
[21] K. Hendrix, M. Vaneynde, G. Koeckelberghs, I.F.J. Vankelecom, Synthesis of modified poly(ether ether ketone) polymer for the preparation of ultrafiltration and nanofiltration membranes via phase inversion, J. Membr. Sci. 447 (2013) 96–106, https://doi.org/10.1016/j.memsci.2013.07.006.
[22] J. Ye, J. Dai, D. Yang, C. Li, Y. Yan, Y. Wang, 2D/2D confinement graphene-supported bimetallic Sulfides/g-C3N4 composites with abundant sulfur vacancies as highly active catalytic self-cleaning membranes for organic contaminants degradation, Chem. Eng. J. 418 (2021), https://doi.org/10.1016/j.cej.2021.129383.
[23] S. Byun, S.H. Davies, A.L. Alpatova, L.M. Corneal, M.J. Baumann, V.V. Tarabara, S. J. Masten, Mn oxide coated catalytic membranes for a hybrid ozonation-membrane filtration: comparison of Ti, Fe and Mn oxide coated membranes for water quality, Water Res. 45 (1) (2011) 163–170, https://doi.org/10.1016/j.watres.2010.08.031.
[24] H. Wu, X. Xu, L. Shi, Y. Yin, L.C. Zhang, Z. Wu, X. Duan, S. Wang, H. Sun, Manganese oxide integrated catalytic ceramic membrane for degradation of organic pollutants using sulfate radicals, Water Res. 167 (2019), 115110, https://doi.org/10.1016/j.watres.2019.115110.
[25] L. Zhang, L. Zhang, Y. Sun, B. Jiang, Porous ZrO2 encapsulated perovskite composite oxide for organic pollutants removal: enhanced catalytic efficiency and suppressed metal leaching, J. Colloid Interface Sci. 596 (2021) 455–467, https://doi.org/10.1016/j.jcis.2021.03.171.
[26] N. Li, G. Chen, J. Zhao, B. Yan, Z. Cheng, L. Meng, V. Chen, Self-cleaning PDA/ZIF-67@PP membrane for dye wastewater remediation with peroxymonosulfate and visible light activation, J. Membr. Sci. 591 (2019), https://doi.org/10.1016/j.memsci.2019.117341.
[27] J. Wang, Z. Wu, T. Li, J. Ye, L. Shen, Z. She, F. Liu, Catalytic PVDF membrane for continuous reduction and separation of p-nitrophenol and methylene blue in emulsified oil solution, Chem. Eng. J. 334 (2018) 579–586, https://doi.org/10.1016/j.cej.2017.10.055.
[28] H. Ma, G. Wang, Z. Miao, X. Dong, X. Zhang, Integration of membrane filtration and peroxymonosulfate activation on CNT@nitrogen doped carbon/Al2O3 membrane for enhanced water treatment: insight into the synergistic mechanism, Sep. Purif. Technol. 252 (2020), https://doi.org/10.1016/j.seppur.2020.117479.
[29] H. Lin, Q. Fang, W. Wang, G. Li, J. Guan, Y. Shen, J. Ye, F. Liu, Prussian blue/PVDF catalytic membrane with exceptional and stable Fenton oxidation performance for organic pollutants removal, Appl. Catal. B 273 (2020), https://doi.org/10.1016/j.apcatb.2020.119047.
[30] J. Gong, J. Liu, X. Chen, Z. Jiang, X. Wen, E. Mijowska, T. Tang, One-pot synthesis of core/shell Co@C spheres by catalytic carbonization of mixed plastics and their application in the photo-degradation of Congo red, J. Mater. Chem. A 2 (20) (2014) 7461–7470, https://doi.org/10.1039/c4ta00173g.
[31] X. Ge, W. Qin, H. Zhang, G. Wang, Y. Zhang, C. Yu, A three-dimensional porous Co@C/carbon foam hybrid monolith for exceptional oil-water separation, Nanoscale 11 (25) (2019) 12161–12168, https://doi.org/10.1039/c9nr02819f.
[32] J. Meng, C. Niu, L. Xu, J. Li, X. Liu, X. Wang, Y. Wu, X. Xu, W. Chen, Q. Li, Z. Zhu, D. Zhao, L. Mai, General oriented formation of carbon nanotubes from metal-organic frameworks, J. Am. Chem. Soc. 139 (24) (2017) 8212–8221, https://doi.org/10.1021/jacs.7b01942.
[33] N. Wang, W. Ma, Z. Ren, Y. Du, P. Xu, X. Han, Prussian blue analogues derived porous nitrogen-doped carbon microspheres as high-performance metal-free peroxymonosulfate activators for non-radical-dominated degradation of organic pollutants, J. Mater. Chem. A 6 (3) (2018) 884–895, https://doi.org/10.1039/c7ta08472b.
[34] S. Liu, L. Zheng, P. Yu, S. Han, X. Fang, Novel composites of α-Fe2O3 tetrakaidecahedron and graphene oxide as an effective photoelectrode with enhanced photocurrent performances, Adv. Funct. Mater. 26 (19) (2016) 3331–3339, https://doi.org/10.1002/adfm.201505554.
[35] Z. Cai, Y. Bi, E. Hu, W. Liu, N. Dwarica, Y. Tian, X. Li, Y. Kuang, Y. Li, X.Q. Yang, H. Wang, X. Sun, Single-crystalline ultrathin Co3O4 nanosheets with massive vacancy defects for enhanced electrocatalysis, Adv. Energy Mater. 8 (3) (2017), https://doi.org/10.1002/aenm.201701694.
[36] X. Li, X. Huang, S. Xi, S. Miao, J. Ding, W. Cai, S. Liu, X. Yang, H. Yang, J. Gao, J. Wang, Y. Huang, T. Zhang, B. Liu, Single cobalt atoms anchored on porous N-doped graphene with dual reaction sites for efficient Fenton-like catalysis, J. Am. Chem. Soc. 140 (39) (2018) 12469–12475, https://doi.org/10.1021/jacs.8b05992.
[37] M. Zhang, C. Xiao, X. Yan, S. Chen, C. Wang, R. Luo, J. Qi, X. Sun, L. Wang, J. Li, Efficient removal of organic pollutants by metal-organic framework derived Co/C yolk-shell nanoreactors: size-exclusion and confinement effect, Environ. Sci. Technol. 54 (16) (2020) 10289–10300, https://doi.org/10.1021/acs.est.0c00914.
[38] H. Wu, T. Inaba, Z.-M. Wang, T. Endo, Photocatalytic TiO2@CS-embedded cellulose nanofiber mixed matrix membrane, Appl. Catal. B 276 (2020), https://doi.org/10.1016/j.apcatb.2020.119111.
[39] Y. Li, S. Li, K. Zhang, Influence of hydrophilic carbon dots on polyamide thin film nanocomposite reverse osmosis membranes, J. Membr. Sci. 537 (2017) 42–53, https://doi.org/10.1016/j.memsci.2017.05.026.
[40] S. Balta, A. Sotto, P. Luis, L. Benea, B. Van der Bruggen, J. Kim, A new outlook on membrane enhancement with nanoparticles: the alternative of ZnO, J. Membr. Sci. 389 (2012) 155–161, https://doi.org/10.1016/j.memsci.2011.10.025.
[41] V. Vatanpour, S.S. Madaeni, A.R. Khataee, E. Salehi, S. Zinadini, H.A. Monfared, TiO2 embedded mixed matrix PES nanocomposite membranes: influence of different sizes and types of nanoparticles on antifouling and performance, Desalination 292 (2012) 19–29, https://doi.org/10.1016/j.desal.2012.02.006.
[42] X. Dong, B. Ren, Z. Sun, C. Li, X. Zhang, M. Kong, S. Zheng, D.D. Dionysiou, Monodispersed CuFe2O4 nanoparticles anchored on natural kaolinite as highly efficient peroxymonosulfate catalyst for bisphenol a degradation, Appl. Catal. B 253 (2019) 206–217, https://doi.org/10.1016/j.apcatb.2019.04.052.
[43] L. Yu, G. Zhang, C. Liu, H. Lan, H. Liu, J. Qu, Interface stabilization of undercoordinated iron centers on manganese oxides for nature-inspired peroxide activation, ACS Catal. 8 (2) (2018) 1090–1096, https://doi.org/10.1021/acscatal.7b03338.
[44] L. Tang, Y. Liu, J. Wang, G. Zeng, Y. Deng, H. Dong, H. Feng, J. Wang, B. Peng, Enhanced activation process of persulfate by mesoporous carbon for degradation of aqueous organic pollutants: electron transfer mechanism, Appl. Catal. B 231 (2018) 1–10, https://doi.org/10.1016/j.apcatb.2018.02.059.
[45] J. Wang, S. Wang, Activation of persulfate (PS) and peroxymonosulfate (PMS) and application for the degradation of emerging contaminants, Chem. Eng. J. 334 (2018) 1502–1517, https://doi.org/10.1016/j.cej.2017.11.059.
[46] M. Sun, I. Zucker, D.M. Davenport, X. Zhou, J. Qu, M. Elimelech, Reactive, self-cleaning ultrafiltration membrane functionalized with iron oxychloride nanocatalysts, Environ. Sci. Technol. 52 (15) (2018) 8674–8683, https://doi.org/10.1021/acs.est.8b01916.
[47] R. Luo, M. Li, C. Wang, M. Zhang, M.A. Nasir Khan, X. Sun, J. Shen, W. Han, L. Wang, J. Li, Singlet oxygen-dominated non-radical oxidation process for efficient degradation of bisphenol a under high salinity condition, Water Res. 148 (2019) 416–424, https://doi.org/10.1016/j.watres.2018.10.087.
[48] C. Chen, T. Ma, Y. Shang, B. Gao, B. Jin, H. Dan, Q. Li, Q. Yue, Y. Li, Y. Wang, X. Xu, In-situ pyrolysis of enteromorpha as carbocatalyst for catalytic removal of organic contaminants: considering the intrinsic N/Fe in enteromorpha and non-radical reaction, Appl. Catal. B Environ. 250 (2019) 382–395, https://doi.org/10.1016/j.apcatb.2019.03.048.
[49] J. Ye, C. Li, L. Wang, Y. Yan, Y. Wang, J. Dai, MOFs derived 3D sea urchin-like carbon frameworks loaded on PVDF membranes as PMS activator for highly efficient bisphenol a degradation, Sep. Purif. Technol. 258 (2021), https://doi.org/10.1016/j.seppur.2020.117669.
[50] H. Wang, W. Guo, B. Liu, Q. Wu, H. Luo, Q. Zhao, Q. Si, F. Sseguya, N. Ren, Edge-nitrogenated biochar for efficient peroxydisulfate activation: an electron transfer mechanism, Water Res. 160 (2019) 405–414, https://doi.org/10.1016/j.watres.2019.05.059.
[51] E.T. Yun, J.H. Lee, J. Kim, H.D. Park, J. Lee, Identifying the nonradical mechanism in the peroxymonosulfate activation process: singlet oxygenation versus mediated electron transfer, Environ. Sci. Technol. 52 (12) (2018) 7032–7042, https://doi.org/10.1021/acs.est.8b00959.
[52] D. Ding, S. Yang, X. Qian, L. Chen, T. Cai, Nitrogen-doping positively whilst sulfur-doping negatively affect the catalytic activity of biochar for the degradation of organic contaminant, Appl. Catal. B 263 (2020), https://doi.org/10.1016/j.apcatb.2019.118348.
[53] P. Hu, M. Long, Cobalt-catalyzed sulfate radical-based advanced oxidation: a review on heterogeneous catalysts and applications, Appl. Catal. B 181 (2016) 103–117, https://doi.org/10.1016/j.apcatb.2015.07.024.
[54] Z. Wang, Y. Du, Y. Liu, B. Zou, J. Xiao, J. Ma, Degradation of organic pollutants by NiFe2O4/peroxymonosulfate: efficiency, influential factors and catalytic

mechanism, RSC Adv. 6 (13) (2016) 11040–11048, https://doi.org/10.1039/c5ra21117d.
[55] M.G. Antoniou, A.A. de la Cruz, D.D. Dionysiou, Degradation of microcystin-LR using sulfate radicals generated through photolysis, thermolysis and e− transfer mechanisms, Appl. Catal. B 96 (3–4) (2010) 290–298, https://doi.org/10.1016/j.apcatb.2010.02.013.
[56] F. Qi, W. Chu, B. Xu, Modeling the heterogeneous peroxymonosulfate/Co-MCM41 process for the degradation of caffeine and the study of influence of cobalt sources, Chem. Eng. J. 235 (2014) 10–18, https://doi.org/10.1016/j.cej.2013.08.113.